Journal of Materials Chemistry C

Accepted Manuscript

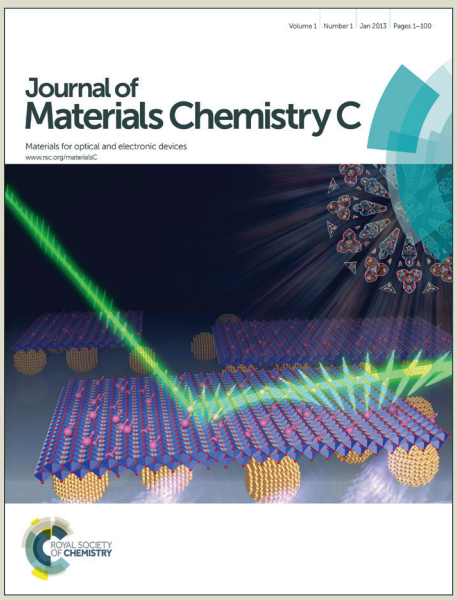

ROYAL SOCIETY OF CHEMISTRY

www.rsc.org/materialsC

Chemical strain effects arising from the large size mismatch between the two A-site cations results in a lowering of the symmetry from polar *R*3*c* to a polar *Cc* in $Bi_{0.95}Dy_{0.05}FeO_3$.

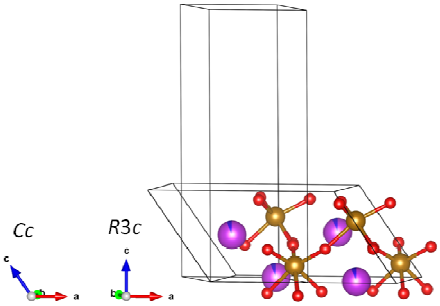

Strain driven structural phase transformations in dysprosium doped $BiFeO_3$ ceramics

Robert C. Lennox[1], Mark C. Price[1], William Jamieson[2], Marek Jura[2], Aziz Daoud-Aladine[2], Claire A. Murray[3], Chiu Tang[3], Donna C. Arnold[1*]

[1] *School of Physical Sciences, University of Kent, Canterbury, Kent, CT2 7NH, UK*

[2] *ISIS Facility, Rutherford Appleton Laboratory-STFC, Chilton, Didcot, Oxfordshire, OX11 0QX, UK*

[3] *Diamond Light Source, Ltd., Harwell Science and Innovation Campus, Didcot, Oxfordshire, OX11 0DE, UK*

[*] *Corresponding Author, Donna C. Arnold, e-mail: d.c.arnold@kent.ac.uk, tel: 01227 827810, fax: 01227 827558*

Abstract

A detailed powder neutron and synchrotron diffraction study coupled with a complementary Raman spectroscopy study of the addition of Dy^{3+} into $BiFeO_3$ ceramics is reported here. It can be seen that the addition of Dy^{3+} destabilises the polar *R*3*c* symmetry due to chemical strain effects arising from the large size mismatch between the two A-site cations (Dy^{3+} and Bi^{3+}). This results in a lowering of the symmetry to a polar *Cc* model and in the range $0.05 \leq x \leq 0.30$ in $Bi_{1-x}Dy_xFeO_3$ competition develops between the strained polar *Cc* and non-polar *Pnma* symmetries with the *Cc* model becoming increasingly strained until approximately x = 0.12 at which point the *Pnma* model becomes favoured. However, phase co-existence between the *Cc* and *Pnma* phases persists to $x = 0.25$. Preliminary magnetic measurements also suggest weak ferromagnetic character which increases in magnitude with increasing Dy^{3+} content. Preliminary electrical measurements suggest that whilst $Bi_{0.95}Dy_{0.05}FeO_3$ is most likely polar; $Bi_{0.70}Dy_{0.30}FeO_3$ shows relaxor-type behaviour.

Introduction

The technological importance of multiferroic materials has lead to resurgence in research in this area. Bismuth ferrite is by far the most widely studied material primarily due to the observation of both room temperature magnetic (T_N ~ 350 – 370 ^oC) and electric ordering (T_c ~ 810 – 830 ^oC).[1] At room temperature $BiFeO_3$ exhibits a distorted perovskite structure with rhombohedral polar *R*3*c* symmetry. At higher temperatures (≥ 820 ^oC) $BiFeO_3$ adopts the

$GdFeO_3$-type *Pbnm* structure[2] and a (probable) orthorhombic γ-phase[3] is observed above 930 °C in a small window before decomposition. The magnetic ordering can be characterised as a G-type antiferromagnet with an incommensurate spin cycloid structure which propagates along the [110] direction with a repeat distance of approximately 62 – 64 nm.[1] However, problems with phase purity, high conductivities and dielectric losses act as a barrier to potential commercial use.

Doping with divalent species, such as Ca^{2+}[4, 5] or trivalent species, such as La^{3+}[6] to realise a canted AFM structure and/or to improve the ferroelectric response is emerging as a viable methodology to overcome some of the issues associated with $BiFeO_3$. In particular doping of the Bi^{3+} A-site of the perovskite with rare earth cations (RE) has received extensive attention, with a variety of symmetries, and magnetic and electric behaviours reported with increasing values of x in $Bi_{1-x}RE_xFeO_3$ and/or decreasing ionic radii of the rare earth cation.[6-10]

Dysprosium as a replacement for bismuth, is particularly interesting since it has been suggested that the addition of Dy^{3+} into $BiFeO_3$ results in an effective suppression of the spin cycloid.[11, 12] However, despite numerous reports within the literature we still possess little understanding of the structural, electronic and magnetic properties on the insertion of Dy^{3+} into the $BiFeO_3$ lattice. Some reports have suggested that the *R*3*c* phase is stable up to x = 0.1,[11, 13, 14] whilst others have suggested much lower limits such as x = 0.075[15] and 0.08[16, 17] as well as higher limits including x = 0.15[18] and 0.20[19] . The nature of this phase transition is also not well understood with non-polar $GdFeO_3$-type *Pnma*,[20-22] polar $Pn2_1a$[23] and antiferroelectric $PbZrO_3$-type *Pbnm*[16, 17] symmetries all suggested.

Whilst the general consensus within the literature suggests that the addition of Dy^{3+} initially improves the ferroelectric and magnetic behaviour in these materials, a full understanding of the structural evolution on the addition of dysprosium and the resulting change in properties remains elusive.[11, 18, 22-24] This is especially important if we are to understand the exciting phenomena recently reported such as enhanced magnetoelectric coupling observed on magnetic poling[11] or the superior remnant polarisation observed in materials annealed in a magnetic field.[25] Much of the controversy in phase analysis arises since the majority of these structural studies are based solely on laboratory based x-ray diffraction data which are inadequate to probe subtle structural distortions and changes in symmetry. Recently the power of powder neutron diffraction studies to unravel the complex structural phase transitions and behaviours in La^{3+} and Nd^{3+} doped $BiFeO_3$ materials has been demonstrated. For example Rusakov *et. al.* reported that $Bi_{1-x}La_xFeO_3$ undergoes a complex

series of composition driven phase transitions. They reported that between $0 \leq x \leq 0.10$ these materials adopt an *R*3*c* $BiFeO_3$-type structure, before transforming to an anti-ferroelectric, $PbZrO_3$-related, phase at $x = 0.18$ ($Bi_{0.82}La_{0.18}FeO_3$). An incommensurately modulated structure is adopted between $x = 0.19$ and $x = 0.30$ before finally transforming to $GdFeO_3$-type *Pnma* structure for $x = 0.30$.[6] In contrast $Bi_{1-x}Nd_xFeO_3$ is reported to have the *R*3*c* structure between $x = 0$ and $x = 0.12$ transforming to the anti-polar $PbZrO_3$-type phase and finally adopting the *Pnma* structure at $x = 0.22$.[8] Anomalous behaviour has also been observed in variable temperature powder neutron diffraction studies performed on $Bi_{0.5}La_{0.5}FeO_3$ (Pnma) where magnetic ordering appears to be responsible for driving octahedral tilting such as to maximise the super-exchange pathway. This magnetostrictive effect is unusual in that it exhibits an increasing in-phase tilt mode with increasing temperature resulting in an Invar effect along the magnetic *c* axis and anisotropic displacement of the Bi^{3+} and La^{3+} along the *a* axis.[7]

In this paper we report a complementary powder neutron diffraction, synchrotron diffraction and Raman spectroscopy study to understand the subtle distortions and structural transitions driven by A-site size variance in $Bi_{1-x}Dy_xFeO_3$ ($0 \leq x \leq 0.30$) materials. We discuss the origin of a complex series of phase transitions which includes a strain driven transition from *R*3*c* to a probable monoclinic phase with a *Cc* space group. We also present magnetic and electric data with the aim of further understanding the complex behaviour in these materials.

Experimental

$Bi_{1-x}Dy_xFeO_3$ materials were prepared using a similar method to that previously reported by us.[2, 3, 26] Stoichiometric ratios of Fe_2O_3, Bi_2O_3 and Dy_2O_3 (all Sigma Aldrich, ≥ 99 %) were reacted for five hours at 800 °C with 6 mol % excess of Bi_2O_3 in order to mitigate against volatilisation of bismuth. The resulting powder contained small amounts of the sillenite (~$Bi_{24}FeO_{39}$) parasitic phase which were removed by leaching with 2.5 M HNO_3 under continuous stirring for two hours, washed with ddH_2O and dried for one hour at 400 °C to yield single phase materials. Phase purity was assessed using a Bruker D8 Advance diffractometer equipped with Cu $K\alpha_1$ radiation (40 kV and 40 mA, λ = 1.54413 Å) over a range of $10 \leq °2\theta \leq 70$.

Room temperature powder neutron diffraction measurements were performed on the high resolution powder diffractometer (HRPD) at the ISIS facility, UK. Data were collected with

the materials loaded into 6 mm diameter cylindrical vanadium cans. Room temperature synchrotron diffraction data were collected on the high resolution diffraction beamline (I11)[27] at the Diamond Light Source, UK (λ = 0.826943(5) Å and 2θ zeropoint = 0.001533(3)). In order to minimise absorption effects, associated with bismuth at the synchrotron radiation energy employed in these experiments and the glass capillaries used, samples were loaded onto the outside surface of 0.3 mm diameter glass capillaries by applying a thin layer of hand cream and rolling the capillary in the sample to provide an even coat of material. All refinements were performed using the General Structure Analysis System (GSAS) suite of programs and are described in more depth in the supplementary information.[28, 29]

Pellets were prepared for Raman spectroscopy and electrical characterisation by pressing the material into 10 mm diameter pellets and sintering at 850 ^{o}C for three hours. Pellets were polished to give a near mirror surface for Raman analysis. It was noted that with increasing Dy^{3+} content it became harder to achieve mirror surfaces on the pellets as mechanical strength of the pellets reduced. For electrical measurements Pt electrodes were applied to a smooth surface using an Emitech K550x sputter coater. Raman spectra were collected on a Horiba Yvon Jobin LabRAM instrument. Room temperature mapping was performed using a 633 nm laser over an area of approximately 50 μm × 50 μm. Measurements were performed using ten integrations with a two second acquisition time with ×50 objective and 600 lines per mm grating (giving a spectral resolution of ± 0.5 cm^{-1}) over a Raman shift range of between 80 cm^{-1} and 1280 cm^{-1}. High resolution Raman spectroscopy was performed with a 633 nm wavelength laser at 77 K using a Linkam Examina THMS 600 cold stage. Measurements were performed using ten integrations with a one second acquisition time with a ×50 objective and 1800 lines per mm grating. Dielectric measurements were made using an Agilent 4294A impedance analyser over a frequency range of approximately 100 Hz – 5 MHz and a temperature range of approximately 50 – 340 K (cooling/heating rates of 2 $Kmin^{-1}$) and applied AC excitation of 500 mV. SQUID magnetometry measurements were performed using a Magnetic Property Measurement System (MPMS) XL-7 instrument. Data were collected over a temperature range of 2 K to 300 K in both zero field and in an applied field of 1000 Oe. Hysteresis behaviour was investigated at 120 K and 300 K in a variable field of approximately (+/-) 70000 Oe using a step size of 100 Oe between 0 and 1000 Oe, 500 Oe between 1000 Oe and 5000 Oe and 5000 Oe between 5000 Oe and 70000 Oe.

Results and Discussion

Crystallographic considerations: Powder XRD (not shown) indicated that single phase materials were prepared at x = 0, 0.02, 0.05 and 0.30 for $Bi_{1-x}Dy_xFeO_3$ materials which appear to crystallise in the parent $BiFeO_3$, *R*3*c* and $DyFeO_3$ *Pnma* symmetries respectively. Between $0.10 \leq x \leq 0.25$ mixed phase *Pnma* and *R*3*c* materials are observed consistent with some of the previous studies.[11, 13, 14, 20-22] More in depth structural studies were performed using powder neutron and synchrotron diffraction experiments. Investigation of the x = 0, 0.02 and 0.05 materials demonstrated reasonable fits to the *R*3*c* space group (see supplementary information). Both the lattice parameters and the cell volume decrease with increasing Dy^{3+} contents as expected from the difference in ionic radii between Dy^{3+} and Bi^{3+} (0.912 Å and 1.03 Å respectively)[30] as shown in Figure 1. However, further inspection of the fits using the *R*3*c* model as well as the goodness of fit factors demonstrate that the *R*3*c* model becomes insufficient to describe both the peak intensities and shape observed in the data (Figures 2 and 3). Furthermore, it can be seen, particularly in the synchrotron diffraction data, that the addition of Dy^{3+} results in a significant broadening of the peaks as also shown in Figures 2 and 3. The origin of peak broadening in materials can arise as a result from size and strain effects and thus warranted further investigation.

Since the broadening is most pronounced in the synchrotron diffraction data, we looked at these refinements in more detail. Initial Rietveld refinements were performed using a psuedo-Voigt function to describe the peak shape (Type 2 profile function in the GSAS suite of programs) which employs a multi-term Simpson's rule integration of the pseudo-Voigt function allowing for the refinement of both Gaussian (GU, GV, GW) and Lorentzian (LX, LY) terms as described by Howard and Thompson *et. al.*[31, 32] One of the advantages of this methodology is that it allows us to probe (through the Lorentzian terms) the effects of strain broadening (LY) and crystallite size broadening (LX). Inspection of the data indicated that crystallite size broadening does not contribute to the broadening observed in these materials, with the LX term consistently refined to zero. Variation of the Lorentzian strain term (LY) indicates a linear increase in LY with increasing Dy^{3+} contents, as shown in Figure 4. In order to investigate the effects of strain, further refinements were performed on $Bi_{0.95}Dy_{0.05}FeO_3$ using an expanded pseudo-Voigt function which includes expanded micro strain broadening terms which are related to the crystal structure (Type 4 profile function in the GSAS suite of programs).[31-35] Close inspection of the data indicated that despite the extra degrees of freedom provided using this method, an improvement in the fit of the *R*3c model to the data was not observed (see supplementary information). This suggests that strain

effects can not be the sole source of the broadening observed with the addition of Dy^{3+} to these materials. When considering peak broadening it is important to consider the effects of compositional variations across crystallites resulting in multiple lattice parameters, on the peak shape. Leineweber *et. al.* reported the use of the Stephen's micro strain broadening to model these types of variations.[36] Since the use of this model (described above) did not improve the description of the peak shape in these materials, coupled with the low Dy^{3+} contents reported, it is unlikely that lattice parameter variations contribute significantly to the peak broadening observed here.

Recently symmetry mode analysis of distortions in materials is emerging as a powerful tool to investigate subtle structural phase transitions.[7, 37-39] In this method the structural distortion is described by different distortion modes, such as octahedral tilts or cation displacements that can be transformed according to different irreproducible representations of the parent space group. This allows for the distortions to be effectively uncorrelated allowing for the contribution of each distortion mode to be investigated. We performed a distortion mode symmetry analysis using the online software ISODISTORT[40, 41] in order to investigate potential distortions of the crystal structure, which may explain the peak broadening observed here. Distortion modes were suggested as Γ3, F, L and T modes resulting in a lowering of the symmetry to either monoclinic, *Cc* or triclinic, *P*1 symmetry. In order to investigate the probability of these models to accurately describe our data, Lebail refinements were performed on both the powder neutron and synchrotron diffraction data for $Bi_{0.95}Dy_{0.05}FeO_3$. The Lebail method allows for the 'best fit' achievable to be realised by allowing for optimal peak intensities to be modelled without taking into account the physical atom positions allowing for the potential distortion modes to be investigated.[42] Inspection of the data shows that the distortion modes F, L and T can be discounted since they result in significant supercell peaks, which are not observed in our data. However, the Γ3 modes (which results in either *P*1 or *Cc* symmetries) provides sensible models to describe our data. It is clear from our Lebail refinements that both space group models result in a significant lowering of the goodness of fit parameters and improved modelling of both the peak shape and peak intensities in our data as shown in Figures 5 and 6, Table 1 and the supplementary information. Interestingly both *P*1 and *Cc* symmetries have recently been proposed for the α-phase of the parent $BiFeO_3$ material.[43, 44] However, whilst the *P*1 model proposed by Wang *et. al.*[43] is strikingly similar to the one proposed through our structural mode analysis we found no evidence for a similar *Cc* model to that proposed by Sosnowska *et. al.*[44] Lebail

refinements with this Cc model were unable to accurately fit both the neutron and synchrotron diffraction data.

In order to further investigate the models determined through symmetry mode analysis, full Rietveld refinements were performed for the diffraction data collected for the $Bi_{0.95}Dy_{0.05}FeO_3$ material as discussed in the supplementary information. Refinements of both the synchrotron and neutron diffraction data in the *P*1 model proved unstable, with unrealistic values observed for some parameters allowing us to further rule out this model. Refinements performed in the *Cc* model yielded better fits to both peak shape and peak intensity profiles for both neutron and synchrotron diffraction data as shown in Figure 7 with full refinement details given in Table 2. When considering a lowering of symmetry it is important to consider if the improvement of the observed fit is significant or limited to an increase in refineable degrees of freedom. Comparison of the goodness of fit parameters achieved for refinements suggest a significant enhancement in the quality of the fit. In order to further investigate the significance of the improved fit Hamilton's significance tests have been employed.[45] These statistical calculations indicated that the improvement in the refinement fits using the *Cc* model were significant at the 0.005 confidence level (*R* factor ratios of 1.29and 1.179 were obtained for synchrotron and neutron diffraction refinements respectively, compared with calculated values of 1.079 and 1.157). It should be noted that the powder neutron diffraction data also contains contributions from magnetic Bragg peaks which have not been modelled. In order to investigate a possible phase transition between $BiFeO_3$ and $Bi_{0.95}Dy_{0.05}FeO_3$ we also performed full refinements on the synchrotron diffraction data collected for the $x = 0$ and $x = 0.02$ materials using the *Cc* model (please see supplementary information). Close inspection of the goodness of fit parameters demonstrate that a significant improvement is observed in both R_{wp} and R_p at around x = 0.03 as shown in Figure 8. Significance tests were also performed on the x = 0 and 0.02 materials suggesting that the improvements in the observed fit were probably not significant at the 0.005 confidence level (*R* factor ratios of 1.087, 1.044 and 1.132 were obtained for synchrotron and neutron diffraction refinements of $BiFeO_3$ and synchrotron refinements of $Bi_{0.98}Dy_{0.02}FeO_3$ respectively, compared with calculated values of 1.048, 1.038 and 1.040). *Cc* symmetry has previously been proposed for Bi containing perovskites and has recently been suggested for the Pb-free ferroelectric, $Na_{0.5}Bi_{0.5}TiO_3$ which interestingly, was originally considered to exhibit *R*3*c* symmetry.[46] The coexistence of both *R*3*c* and *Cc* phases has also been reported for related $Na_{0.5}Bi_{0.5}TiO_3$-$BaTiO_3$ materials.[47] The model determined from our symmetry mode analysis is consistent with the models proposed for $Na_{0.5}Bi_{0.5}TiO_3$.[46, 48] The rhombohedral *R*3*c* model can be

described as having anti-phase tilting in the *x*, *y* and *z* directions, denoted by the Glazer notation $a^-a^-a^-$, with the ferroelectric polarisation along the $[111]_{pseudocubic}$ direction.[1, 49] The monoclincic distortion results in an $a^-a^-c^-$ tilt system such that, whilst all the tilts remain anti-phase, the magnitude of the tilt in the *z*-direction is unique.[46] However, in contrast the ferroelectric axis now lies along the $[110]_{pseudocubic}$ direction.[48] This implies that the addition of Dy^{3+} onto the Bi^{3+} site results in a rotation of the polarisation vector. A schematic representation of the *R*3*c* and *Cc* unit cells is given in Figure 9. We further investigated our mode analysis data to probe the amplitude of the Γ3 tilt on the atomic sites in order to further enhance our understanding of the driving forces for the subtle phase transition, as shown in the supplementary information. It is clear from these data that the distortion mode has the largest effects on the O1 and O3 sites i.e. the equatorial oxygen sites resulting in a distortion of the FeO_6 octahedra and ultimately a change in the polarisation axis. Furthermore, the change in symmetry clearly results in a lowering of the Lorentizian strain term, LY, potentially making *Cc* symmetry more favourable. We suggest that the most likely driving force for this transition is chemical strain induced by the large A-site size variance between Dy^{3+} and Bi^{3+}. However, the complex interplay between magnetic and possible ferroelectric order parameters may also play a significant role in driving this phase transition (as discussed in more detail below) and we are currently investigating this further.

Variable composition studies ($0.05 \geq x \geq 0.25$) using both powder neutron and synchrotron X-ray diffraction indicates the formation of small amounts of secondary phase at Dy^{3+} contents as low as $x = 0.05$ consistent with the work by Sun *et.al.* and Troyanchuk and co-workers.[15-17] These diffraction data can clearly be modelled using a combination of polar *Cc* and non-polar *Pnma* symmetries as shown in the supplementary information. We found no evidence for the formation of the previously reported $PbZrO_3$-type antiferroelectric phases in any of our data.[23] Interestingly refinements indicate that Dy^{3+} continues to dope into the *Cc* phase with the lattice parameters and cell volume continuing to decrease with increasing dysprosium contents. The Lorentzian strain term, LY, continues to increase, before reaching a plateau at approximately $x = 0.12$ before dropping sharply (Figure 10). This is consistent with the monoclinic phase becoming far less tolerant of dysprosium, with the cell volume and lattice parameters indicating that no more dysprosium is incorporated into the lattice. This suggests that the most strained material in the monoclinic phase is at approximately x = 0.12 and that perhaps if a single phase material could be obtained it could be expected to show enhanced properties. This is consistent with Li *et. al.* whom reported that the best electrical properties were observed in $Bi_{0.90}Dy_{0.10}FeO_3$ materials.[24] In addition the large A-site

variance between Bi^{3+} and Dy^{3+} leads to a structural instability within the *Pnma* phase which results in phase segregation with multiple *Pnma* phases with varying lattice constants observed in data $x \geq 0.18$. No coherent trend is observed in the lattice parameters (not shown) for either phase this is most likely due to the increasing complexity of the data with increasing A-site variance such that phase segregation of the Bi^{3+} and Dy^{3+} cations leads to multiple phases showing slight variations in lattice parameters. In contrast with the literature a single *Pnma* phase was not obtained until $x = 0.30$.[18-22] However close inspection of both the powder neutron and synchrotron diffraction data indicates a severe anisotropic 'tailing' of the peaks. Modelling these data to include an additional *Cc* phase (i.e. the phase transformation between *Cc* and *Pnma* symmetries is incomplete) did not accurately model this broadening. The most accurate model arises by considering two different *Pnma* phases with slightly different lattice parameters (Figure 11) suggesting phase segregation of the Dy^{3+} and Bi^{3+} cations across crystallites. Due to absorption effects with both Dy^{3+} and Bi^{3+} in neutron and synchrotron diffraction experiments respectively, it was not possible to accurately investigate the fractional occupancies and thus the distribution of Dy^{3+} and Bi^{3+} cations in these phases. Further inspection of the powder neutron data suggests evidence for diffuse scattering, perhaps suggesting polar nanoregions (discussed in more detail below). This may suggest that, in fact, a mixture of non-polar *Pnma* and the equivalent polar $Pn2_1a$ symmetries is perhaps more appropriate, but it was not possible to differentiate between these two space groups from these data. Given our structural studies we therefore propose the phase diagram shown in Figure 12 for Dy^{3+} doped $BiFeO_3$ materials.

Raman Analysis: Raman mapping analysis of the $Bi_{1-x}Dy_xFeO_3$ ceramics ($0 \leq x \leq 0.30$) was performed at room temperature and mapped over a region of approximately 50 × 50 μm using a 633 nm wavelength laser. Below $x = 0.05$ and for $x = 0.30$ single phase materials with $BiFeO_3$ type and $LaFeO_3$ type spectra were obtained respectively. Between $0.05 \leq x \leq 0.30$ elements of both spectra were clearly evident, confirming the mixed phase nature of these materials. Phase maps were prepared by selecting peaks which are attributable to either the *R*3*c*/*Cc* or *Pnma* phases. Limits were set in the Raman shift between approximately 100 and 160 cm^{-1} and 560 and 660 cm^{-1} to define contributions from the *R*3*c*/*Cc* and *Pnma* phases respectively. It is clear from the spectra that the ratio between *Cc* (polar) and *Pnma* (non polar) phases increases with increasing Dy^{3+} content, consistent with our observations from powder diffraction studies as shown in Figure 13. High resolution single point data was also collected at 80 K in order to further investigate these materials. It can be seen that our spectra

are in excellent agreement with the extensive studies reported in the literature.[9, 50] Using the assignments derived by Hlinka *et. al.* and Bielecki *et.al.* we can assign the modes observed in our spectra as shown in Figure 14 and Table 3. The spectra for $x = 0$ and $x = 0.02$ are very similar, with both showing sharp peaks which are easily attributable to modes associated with the *R*3*c* phase. Small shifts in peak position are observed with the addition of Dy^{3+}, consistent with changes in the unit cell. A much larger shift is observed in the peak assigned to the A_1 tilt mode from 224.2 cm^{-1} to 227.1 cm^{-1} in $BiFeO_3$ and $Bi_{0.98}Dy_{0.02}FeO_3$ respectively. This is consistent with the observations of Bielecki *et. al.* for Tb^{3+} and Sm^{3+} doped $BiFeO_3$ materials who attribute this shift to a changes in the oxygen tilt angle along the [111].[9] Calculation of the oxygen octahedral rotation, ω, from powder synchrotron diffraction data gave negligible difference within error in the values calculated for $BiFeO_3$ (12.2°) and $Bi_{0.98}Dy_{0.02}FeO_3$ (12.2°) respectively consistent with only a slight increase in Raman shift.[51] In contrast $Bi_{0.95}Dy_{0.05}FeO_3$ shows subtle deviations and peak broadening when compared to that obtained for $BiFeO_3$ (Figure 14). Close inspection of the spectrum suggests the loss of some of the phonon modes expected to be associated with *R*3*c* symmetry supporting the suggestion of a subtle change in symmetry from *R*3*c* to *Cc* as observed in powder diffraction studies. It is evident that there is a large shift in the octahedral tilt mode from 224.2 cm^{-1} to 236.7 cm^{-1} in $BiFeO_3$ and $Bi_{0.95}Dy_{0.05}FeO_3$ respectively. Whilst similarly large shifts have been observed for Tb- and Sm-doped $BiFeO_3$ materials without a change in symmetry, we suggest that rather than argue against a change in symmetry this demonstrates a large increase in the octahedral tilt observed in this material as a result of changing symmetry.[9] Furthermore, the E(1) mode in $BiFeO_3$ at approximately 75 cm^{-1} can be attributed to an antiphase vibration between the A-site and the FeO_6 sublattices. In previous reports this feature shifts very little and has become less pronounced, or disappeared completely on doping.[9] In contrast in $Bi_{0.95}Dy_{0.05}FeO_3$ this feature becomes very pronounced and shifts dramatically from 75.1 cm^{-1} to 85 cm^{-1}. In addition a shoulder becomes evident at a Raman shift of approximately 100 cm^{-1} further suggestive of a subtle phase transition related to both the A-site cation variance and tilt of the FeO_6 lattice. The Raman spectrum collected for the $Bi_{0.70}Dy_{0.30}FeO_3$ (Figure 13) is characterised by broad peaks and is consistent with other rare earth doped $BiFeO_3$ materials which crystallise with *Pnma* symmetry such as $Bi_{0.5}La_{0.5}FeO_3$.[9, 52, 53] Assignments to the phonon modes (Table 3) were based on the observations of Bielecki *et. al.* for Tb^{3+} and Sm^{3+} doped $BiFeO_3$ ceramics.[9]

Electric and Magnetic Characterisation: Magnetic field dependence data collected at room temperature for both the $Bi_{0.95}Dy_{0.05}FeO_3$ and $Bi_{0.70}Dy_{0.30}FeO_3$ materials showed evidence for weak ferromagnetism which increased substantially in magnitude on increasing Dy^{3+} contents as shown in Figure 15 consistent with previous reports.[11, 18-21] It is clear that in both cases that the hysteresis loops do not fully saturate. This lack of saturation has been suggested to arise as a result of magnetisation effects of the iron sublattice on the paramagnetic Dy^{3+} cations.[18] The remnant magnetisation was determined to be 0.039 emu/g, 0.035 emu/g, 0.548 emu/g and 0.367 emu/g for $Bi_{0.95}Dy_{0.05}FeO_3$ and $Bi_{0.70}Dy_{0.30}FeO_3$ at 120 K and 300 K respectively, comparable with the values obtained from previous studies.[11, 18, 20] Zero field cooled(ZFC)/Field cooled (FC) measurements collected between 5 K and 300 K show a clear Curie tail with no evidence of deviation between the ZFC/FC data, confirming that antiferromagnetic character is retained in both materials. It has been suggested that Dy^{3+} substitution into the $BiFeO_3$ lattice results in a substitution-driven modification of the incommensurate G-type spin cycloid to a collinear G-type anti-ferromagnetic structure, in which the magnetic spins are canted and a small net magnetic moment becomes measurable.[18] In order to further investigate the origins of the weak ferromagnetic character observed here, we considered the magnetic Bragg reflections observed at room temperature in our powder neutron diffraction data. Comparison of the powder neutron diffraction data for $BiFeO_3$ and $Bi_{0.95}Dy_{0.05}FeO_3$ shows clear similarities between the position and intensity (not refined) of the magnetic Bragg peaks, suggesting that the spin cycloid is retained (supplementary information). This is contradictory to the field dependence data which would be expected to show a linear field dependence of the magnetisation if the spin cycloid is retained.[9] Since small amounts of parasitic phases, such as Fe_2O_3 can give rise to a SQUID response, we further inspected our data for the possibility of impurity phases; however, we found no evidence for such phases in our diffraction data. Previously, the formation of magnetic clusters in doped $CaMnO_3$ perovskites has been proposed.[54] In these materials ferromagnetic clusters form in an antiferromagnetic matrix resulting in the observation of weak ferromagnetic character, with small values of remnant magnetisation. It is possible that small canted antiferromagnetic or ferromagnetic clusters are forming leading to the field dependent magnetisation observed, whilst the long range spin cycloid structure remains intact on average as observed in the powder neutron diffraction data. The origin of the magnetic behaviour in $Bi_{0.70}Dy_{0.30}FeO_3$ was again investigated by close inspection of the powder diffraction data. As with $Bi_{0.95}Dy_{0.05}FeO_3$ we found no evidence for the presence of parasitic magnetic phases which may give rise to the observed weak ferromagnetic character. It should

be noted that it is not possible to entirely rule out the presence of parasitic phases in our powder neutron diffraction data due to the high backgrounds resulting from absorption effects arising from dysprosium. However, since we have both high resolution synchrotron and neutron data we believe this to be unlikely. Investigation of the magnetic Bragg peaks again showed some similarities to those observed for the parent $BiFeO_3$ material (particularly the peak at a *d*-spacing of approximately 4.6 Å). Previous magnetic structure studies on other rare earth doped materials have shown that this peak is retained when the material transitions to a collinear G-type antiferromagnet, consistent with the larger remnant polarisation observed for this material.[7, 8] It is therefore probable that the addition of Dy^{3+} results in the loss of the magnetic spin cycloid on entering the non-polar *Pnma* phase but further work is required to fully understand the magnetic structure in this material.

Preliminary electrical measurements for $Bi_{0.95}Dy_{0.05}FeO_3$ indicates an anomaly in the dielectric data at a temperature of 675 K consistent with a transition from antiferromagnetic to paramagnetic behaviour, which is in reasonably good agreement with the transition temperature observed for the parent $BiFeO_3$ material as shown in Figure 16.[1] Despite repeated attempts to collect frequency dependent data to investigate the expected ferroelectric-paraelectric phase transition in this material, all data showed high permittivity relaxor-like character typical of non-ohmic electrode effects arising from the 'leaky' dielectric characteristics of the material.[55, 56] The 'leaky' nature of this material also prevented us from collecting polarisation-field data. It is therefore difficult to confirm the polar nature of this material, suggested in our diffraction experiments, directly through these measurements. However, it may be worth noting that variable temperature neutron diffraction experiments (not reported here) suggest a phase transition from *Cc* to *Pnma* symmetries at approximately 850 K (this will be discussed in a subsequent manuscript) coincident with the non-ohmic electrode transition observed here, so it may be possible that the potential ferroelectric-paraelectric transition may be masked by electrode effects in this material. Electrical data collected for $Bi_{0.70}Dy_{0.30}FeO_3$ again shows an anomaly in the dielectric constant at a temperature of approximately 700 K, suggestive of a transition from a magnetically ordered to a paramagnetic state (Figure 16), consistent with observations for other rare earth doped $BiFeO_3$ ceramics.[7] Low temperature dielectric measurements demonstrate a frequency dependence of the dielectric constant and the dielectric loss at approximately 100 K (Figure 14) characteristic of relaxor-type behaviour. This may be due to the formation of polar nano-regions which is consistent with both the mixed phase nature and the presence of diffuse scattering in our powder diffraction data. This would seem to also be

consistent with the polarisation-electric field hysteresis loops observed by Khomchenko *et. al.* using piezoforce microscopy.[23] However, these field dependent electrical data were collected at room temperature for a $Bi_{0.90}Dy_{0.10}FeO_3$ material and thus it is unlikely that the origin of the response is from a *Pnma* phase, but more probable it arises from some residual *R*3*c*(*Cc*) phase. In addition to the relaxor-type character, an additional anomaly is observed at approximately 50 K, the origin of which is unknown. Recently $DyFeO_3$ has been shown to undergo a spin re-orientation (Morin) transition at 50 K and thus this anomaly warrants further investigation.[57]

Conclusions

In summary we report here a comprehensive structural study of Dy^{3+} doped $BiFeO_3$ ceramics. We demonstrate a compositional driven phase transition from polar *R*3*c* to polar *Cc* symmetry at approximately $x = 0.03$ which results in a rotation of the polarisation axis from along the [111] in *R*3*c* to along the [110] axis in *Cc*. Single phase *Cc* symmetry is highly strained and is only observed in a small composition window, and a further phase transformation to non polar *Pnma* is observed with a phase co-existence between approximately $0.05 \leq x \leq 0.30$. Furthermore, the large A-site variance between Bi^{3+} and Dy^{3+} means a single Pnma phase is not truly observed at $x = 0.30$ with a more accurate description of the material given by multiple Pnma phases (with differing lattice parameters) arising as a result phase segregation. It should also be noted however, that whilst we suggest *Cc* is the most probably symmetry we cannot rule out the existence of a complex incommensurately modulated structure. We suggest that the large A-site size variance observed between Bi^{3+} and Dy^{3+} results in chemical strain which drives the phase transitions from *R*3*c* – *Cc* – *Pnma*.

Magnetic data suggests that the G-type antiferromagnetic spin cycloid is maintained in $Bi_{0.95}Dy_{0.05}FeO_3$ with the weak ferromagnetic character observed in field dependent magnetisation measurements most likely arising as a result of the formation of magnetic clusters within the material. This is particularly interesting since the spin cycloid is expected to propagate along the [110] direction, which is coincident with the polarisation axis expected from *Cc* symmetry and we are currently investigating this further. In contrast the spin cycloid is suppressed in $Bi_{0.70}Dy_{0.30}FeO_3$ with the material most likely adopting a G-type antiferromagnetic collinear structure. For both materials electrical data suggests magnetic transition temperatures of approximately 675 K consistent with both $BiFeO_3$ and other rare earth orthoferrites. Whilst the dielectric constant measurements for $Bi_{0.95}Dy_{0.05}FeO_3$ were

inconsistent due to non-ohmic electrode effects, $Bi_{0.70}Dy_{0.30}FeO_3$ exhibits low temperature relaxor-type behaviour.

These results clearly demonstrate the importance of using complementary techniques in order to unravel complex behaviour in doped $BiFeO_3$ materials as well as the emerging power of symmetry mode analysis to understand the driving forces.

Acknowledgements

DCA and RCL would like to thank South East Physics Network (SEPnet) for the provision of a PhD studentship. RCL would like to thank Nikitas Gidopoulos. We thank the STFC for facilities access and Diamond Light Source and the ISIS neutron facility for access to I11 (EE3806-1) and HRPD (RB1120366 and RB1220342) beamlines respectively. DCA would also like to thank Dr Finlay Morrison at the University of St Andrews for access to electrical measurement equipment, Dr Emma McCabe for helpful discussion and Dr Christopher Kavanagh, Jonathan Gardner, Richard Hamlyn, Marc Williams, Laura Vera Stimpson and Daniel Jackson for their contributions.

Notes and References

Electronic Supplementary Information (ESI) available: [Supplementary information includes full details of all GSAS refinements performed including full refinement profiles and refinement data. Supplementary information also includes graphical representation of the atomic site amplitudes from our symmetry mode analysis and comparative plots for the magnetic Bragg peaks observed for $BiFeO_3$ and $Bi_{0.95}Dy_{0.05}FeO_3$ in powder neutron diffraction data]. See DOI: 10.1039/b000000x/
CIF files are also available for $BiFeO_3$ in the *R*3*c* model and $Bi_{0.95}Dy_{0.05}FeO_3$ in the *Cc* model. See DOI: 10.1039/b000000x/

[1] G. Catalan, J. F. Scott, *Adv. Mater.* **2009**, *21*, 2463.
[2] D. C. Arnold, K. S. Knight, F. D. Morrison, P. Lightfoot, *Phys. Rev. Lett.* **2009**, *102*, 027602.
[3] D. C. Arnold, K. S. Knight, G. Catalan, S. A. T. Redfern, J. F. Scott, P. Lightfoot, F. D. Morrison, *Adv. Funct. Mater.* **2010**, *20*, 2116.
[4] N. Maso, A. R. West, *Chem. Mater.* **2012**, *24*, 2127.

[5] W.-T. Chen, A. J. Williams, L. Ortega-San-Martin, M. Li, D. C. Sinclair, W. Zhou, J. P. Attfield, *Chem. Mater.* **2009**, *21*, 2085.

[6] D. A. Rusakov, A. M. Abakumov, K. Yamaura, A. A. Belik, G. Van Tendeloo, E. Takayama-Muromachi, *Chem. Mater.* **2011**, *23*, 285.

[7] C. M. Kavanagh, R. J. Goff, A. Daoud-Aladine, P. Lightfoot, F. D. Morrison, *Chem. Mater.* **2012**, *24*, 4563.

[8] I. Levin, M. G. Tucker, H. Wu, V. Provenzano, C. L. Dennis, S. Karimi, T. Comyn, T. Stevenson, R. I. Smith, I. M. Reaney, *Chem. Mater.* **2011**, *23*, 2166.

[9] J. Bielecki, P. Svedlindh, D. T. Tibebu, S. Cai, S.-G. Eriksson, L. Borjesson, C. S. Knee, *Phys. Rev. B.* **2012**, *86*, 184422.

[10] S. Saxin, C. S. Knee, *Dalton Trans* **2011**, *40*, 3462.

[11] P. Uniyal, K. L. Yadav, *J. Phys.: Condens. Matter* **2009**, *21*, 012205.

[12] J. W. Lin, Y. H. Tang, C. S. Lue, J. G. Lin, *Appl. Phys. Lett.* **2010**, *96*, 232507.

[13] W.-M. Zhu, L. W. Su, Z.-G. Ye, W. Ren, *Appl. Phys. Lett.* **2009**, *94*, 142908.

[14] S. K. Barber, S. Jangid, M. Roy, F. C. Chou, *Ceramics International* **2013**, *39*, 5359.

[15] I. O. Troyanchuk, D. V. Karpinsky, M. V. Bushinsky, O. S. Mantytskaya, N. V. Tereshko, V. N. Shut, *J. Am. Ceram. Soc.* **2011**, *94*, 4502.

[16] C. Sun, X. Chen, J. Wang, G. Yuan, J. Yin, Z. Liu, *Solid State Communications* **2012**, *152*, 1194.

[17] C. Sun, Y. Wang, Y . Yang, G. Yuan, J. Yin, Z. Liu, *Materials Letters* **2012**, *72*, 160.

[18] V. A. Khomchenko, D. V. Karpinsky, A. L. Kholkin, N. A. Sobolev, G. N. Kakazei, J. P. Araujo, I. O. Troyanchuk, B. F. O. Costa, J. A. Paixao, *J. Appl. Phys.* **2010**, *108*, 074109.

[19] J. Xu, G. Wang, H. Wang, D. Ding, Y. He, *Materials Letters* **2009**, *63*, 855.

[20] S. Zhang, L. Wang, Y. Chen, D. Wang, Y. Yao, Y. Ma, *J. Appl. Phys.* **2012**, *111*, 074105.

[21] S. Zhang, W. Luo, D. Wang, Y. Ma, *Materials Letters* **2009**, *63*, 1820.

[22] V. A. Khomchenko, I. O. Troyanchuk, M. V. Bushinsky, O. S. Mantytskaya, V. Sikolenko, J. A. Paixao, *Materials Letters* **2011**, *65*, 1970.

[23] V. A. Khomchenko, J. A. Paixao, D. A. Kiselev, A. L. Kholkin, *Mat. Res. Bull.* **2010**, *45*, 416.

[24] Y. Li, J. Yu, J. Li, C. Zheng, Y. Wu, Y. Zhao, M. Wang, Y. Wang, *J. Mater. Sci.: Mater Electron* **2011**, 323.

[25] S. Zhang, Y. Yao, Y. Chen, D. Wang, X. Zhang, S. Awaji, K. Watanabe, Y. Ma, *J. Magnetism and Magnetic Materials* **2012**, *324*, 2205.

[26] G. D. Achenbach, *J. Am. Ceram. Soc.* **1967**, *50*, 437.

[27] S. P. Thompson, J. E. Parker, J. Potter, T. P. Hill, T. M. Cobb, F. Yuan, C. C. Tang, *Rev. Sci. Instrum.* **2009**, *80*, 075107.

[28] A. C. Larson, R. B. V. Dreele, *Los Alamos National Laboratory Report LAUR* **96**, *86*.

[29] B. H. Toby, *J. Appl. Cryst.* **2001**, *34*, 210.

[30] R. D. Shannon, *Acta Cryst.* **1976**, *A32*, 751.

[31] C. J. Howard, *J. Appl. Cryst.* **1982**, *15*, 615.

[32] P. Thompson, D. E. Cox, J. B. Hastings, *J. Appl. Cryst.* **1987**, *20*, 79.

[33] B. van Laar, W. B. Yelon, *J. Appl. Cryst.* **1984**, *17*, 47.

[34] L. W. Finger, D. E. Cox, A. P. Jephcoat, *J. Appl. Cryst.* **1994**, *27*, 892.

[35] P. Stephens, *J. Appl. Cryst.* **1999**, *32*, 281.

[36] A. Leineweber, E. J. Mittemeijer, *J. Appl. Cryst.* **2004**, *37*, 123.

[37] A. J. Tuxworth, E. E. McCabe, D. G. Free, S. J. Clark, J. S. O. Evans, *Inorg. Chem.* **2013**, *52*, 2078.

[38] J. M. Perez-Mato, D. Orobengoa, M. I. Aroya, *Acta Cryst.* **2010**, *A6*, 558.

[39] O. Clemens, F. J. Berry, A. J. Wright, K. S. Knight, J. M. Perez-Mato, J. M. Igartua, O. R. Slater, *J. Solid State Chem.* **2013**, *206*, 158.

[40] B. J. Campbell, H. T. Stokes, D. E. Tanner, D. M. Hatch, *J. Appl. Cryst.* **2006**, *39*, 607.

[41] S. ISOTROPY Software, *iso.byu.edu*.

[42] A. Lebail, H. Duroy, J. J. Fourquet, *Mat. Res. Bull.* **1988**, *23*, 447.

[43] H. Wang, C. Yang., J. Yu, M. Wu, J. Su, K. Li, J. Zhang, G. Li, T. Jin, T. Kamiyama, F. Liao, J. Lin, Y. Wu, *Inorg. Chem.* **2013**, *52*, 2388.

[44] I. Sosnowska, R. Prezenioslo, A. Palewicz, D. Wardecki, A. Fitch, *J. Phys. Soc. Jap.* **2012**, *81*, 044604.

[45] W. C. Hamilton, *Acta Cryst.* **1965**, *18*, 502.

[46] E. Aksel, J. S. Forrester, J. L. Jones, P. A. Thomas, K. Page, M. R. Suchomel, *Appl. Phys. Lett.* **2011**, *98*, 152901.

[47] R. Garg, B. Narayana, A. Senyshyn, P. S. R. Krishna, R. Ranjan, *Phys. Rev. B.* **2013**, *88*, 014103.

[48] B. N. Rao, R. Ranjan, *Phys. Rev. B.* **2012**, *86*, 134103.

[49] A. M. Glazer, *Acta Cryst.* **1972**, *B28*, 3384.

[50] J. Hlinka, J. Porkorny, S. Karimi, I. M. Reaney, *Phys. Rev. B.* **2011**, 020101.

[51] H. D. Megaw, C. N. W. Darlington, *Acta Cryst.* **1975**, *E31*, 161.

[52] J. Andreasson, J. Holmlund, C. S. Knee, M. Kall, L. Borjesson, S. Naler, J. Backstrom, M. Rubhausen, A. K. Azad, S.-G. Eriksson, *Phys. Rev. B.* **2007**, *75*, 104302.

[53] J. Andreasson, J. Holmlund, R. Rauer, M. Kall, L. Borjesson, C. S. Knee, A. K. Eriksson, S.-G. Eriksson, M. Rubhausen, R. P. Chaudhury, *Phys. Rev. B.* **2008**, *78*, 235103.

[54] Y. Wang, Y. Su, X. Wang, W. Su, X. Liu, *J. Appl. Phys.* **2010**, *108*, 063928.

[55] M. Li, A. Feteira, D. C. Sinclair, *J. Appl. Phys.* **2009**, *105*, 114109.

[56] M. Li, D. C. Sinclair, A. R. West, *J. Appl. Phys.* **2011**, *109*, 084106.

[57] B. Rajeswaran, D. Sanyal, M. Chakrabarti, Y. Sundarayya, A. Sundaresan, C. N. R. Rao, *EPL* **2013**, *101*, 17001.

[58] K. Momma, F. Izumi, *J. Appl. Cryst.* **2011**, *44*, 1272.

List of Figures

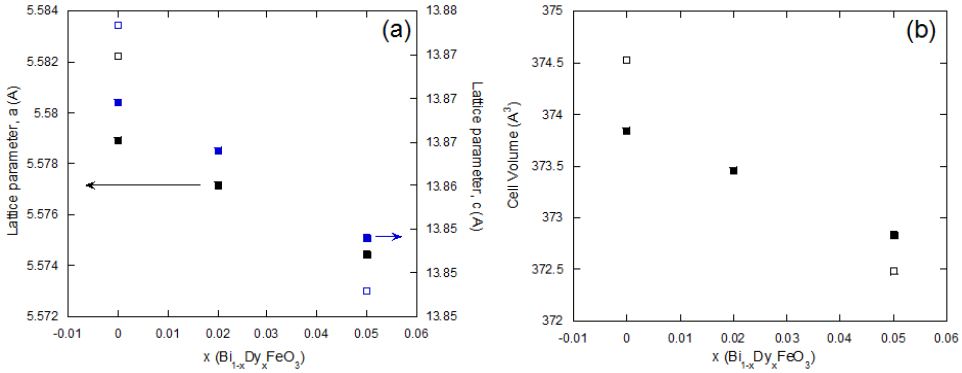

Figure 1: *Variations of (a) lattice parameters a and c, and (b) cell volume with x in* $Bi_{1-x}Dy_xFeO_3$*. Filled and open squares represent the Rietveld refinement of the data collected from powder synchrotron and neutron diffraction respectively (error bars are smaller than the symbol size).*

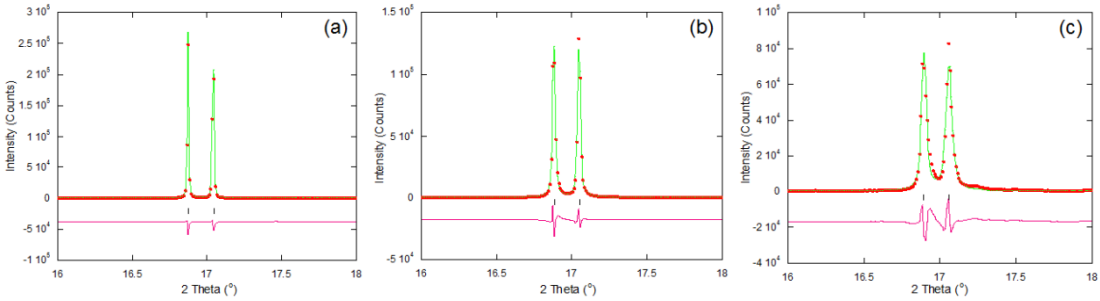

Figure 2: *Rietveld refinement profiles (between* 16^o *and* 18^o 2θ*) for data fitted using the R3c model to synchrotron diffraction data collected for (a)* $BiFeO_3$*, (b)* $Bi_{0.98}Dy_{0.02}FeO_3$ *and (c)* $Bi_{0.95}Dy_{0.05}FeO_3$ *showing increasing peak broadening and limitations of the R3c model with increasing* Dy^{3+} *contents. The red circles represent the observed data, the green line represents the calculated model and the pink line represents the difference. Full refinements are given in the supplementary information.*

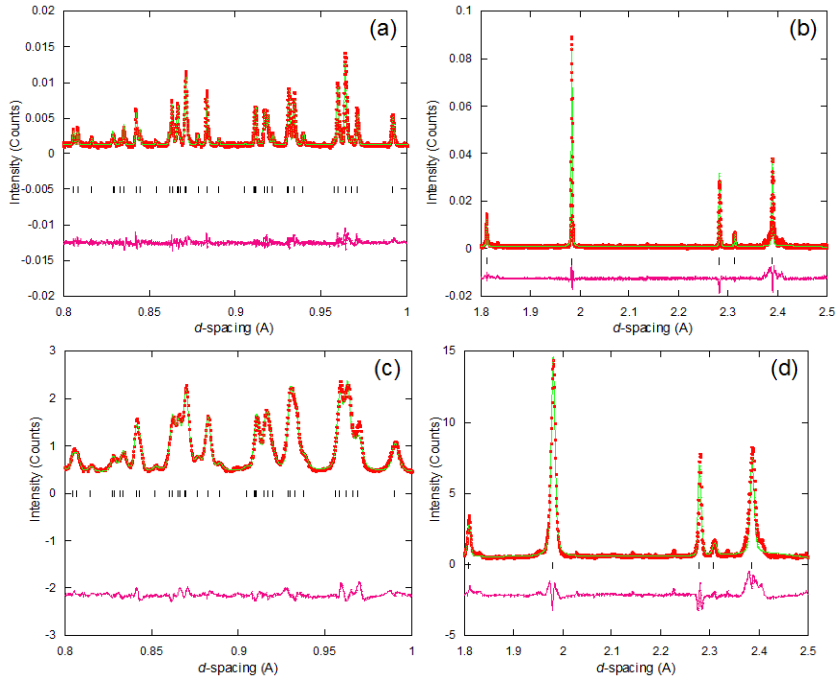

Figure 3: *Rietveld refinement profiles for data fitted using the R3c model to neutron diffraction data collected for $BiFeO_3$ shown between (a) 0.8 Å and 1.0 Å and (b) 1.8 Å and 2.5 Å and $Bi_{0.95}Dy_{0.05}FeO_3$ shown between (c) 0.8 Å and 1.0 Å and (d) 1.8 Å and 2.5 Å showing increasing peak broadening and limitations of the R3c model with increasing Dy^{3+} content. The red circles represent the observed data, the green line represents the calculated model and the pink line represents the difference. Full refinements are given in the supplementary information.*

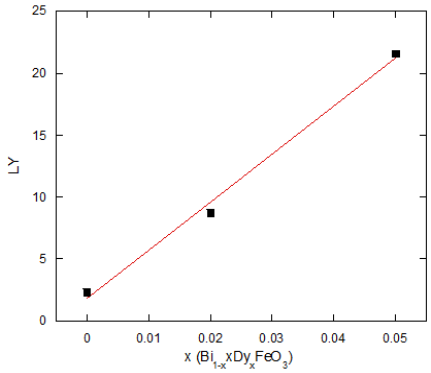

Figure 4: *Variations of the Lorentzian strain term, LY with increasing values of x in $Bi_{1-x}Dy_xFeO_3$ (error bars are smaller than the symbol size).*

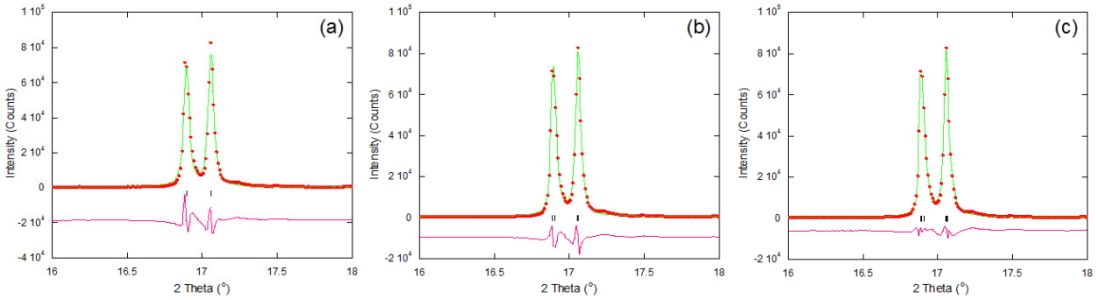

Figure 5: *Lebail refinement profiles between 16° and 18° 2θ for the synchrotron diffraction data collected for* $Bi_{0.95}Dy_{0.05}FeO_3$ *fitted in (a) R3c, (b) Cc and (c) P1 symmetries as determined from symmetry mode analysis showing improved fits for both peak shape and intensity. The red circles represent the observed data, the green line represents the calculated model and the pink line represents the difference. Full refinements are given in the supplementary information.*

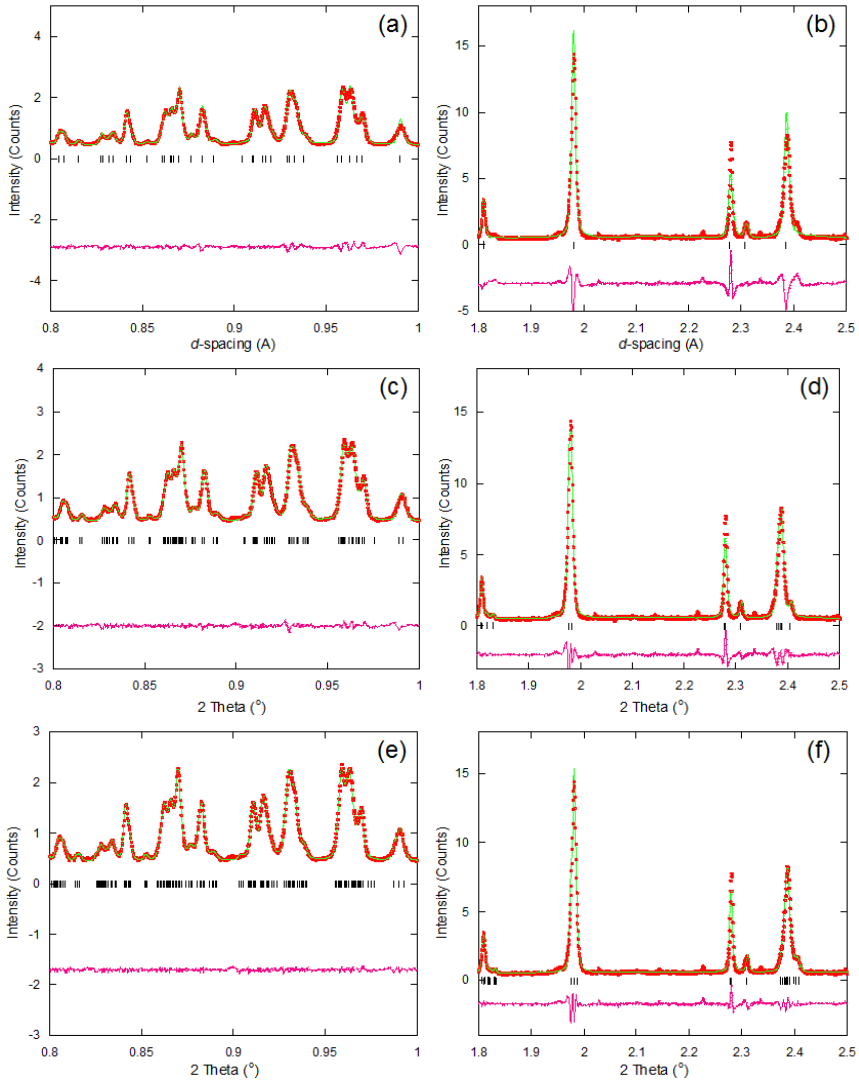

Figure 6: *Lebail refinement profiles between 0.8 Å and 1.0 Å and 1.8 Å and 2.5 Å for the neutron diffraction data collected for* $Bi_{0.95}Dy_{0.05}FeO_3$ *fitted in R3c ((a) and (b)), Cc ((c) and (d)) and P1 ((e) and (f)) symmetries as determined from symmetry mode analysis showing improved fits for both peak shape and intensity. The red circles represent the observed data, the green line represents the calculated model and the pink line represents the difference. Full refinements are given in the supplementary information.*

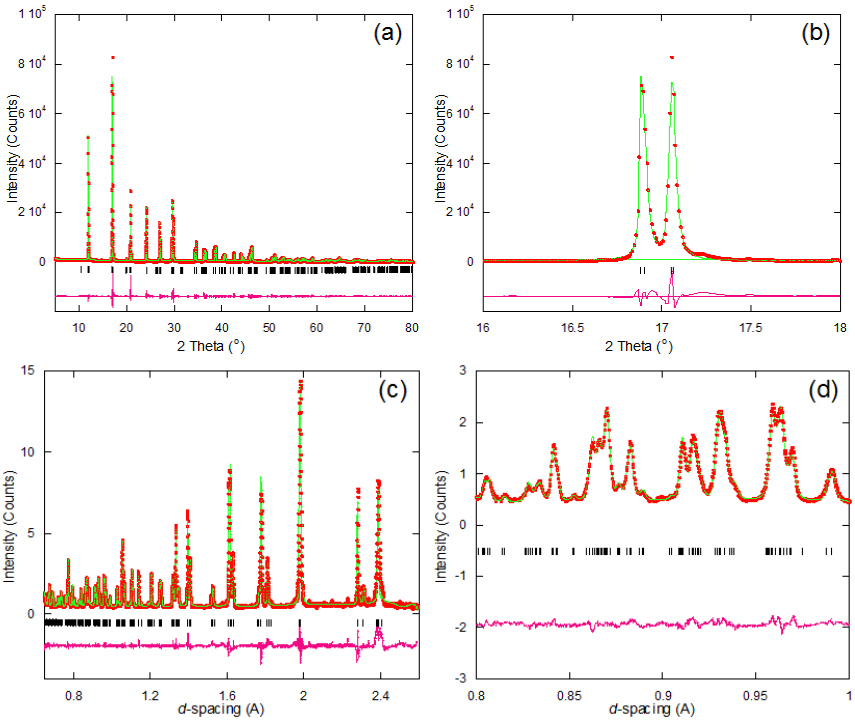

Figure 7: *Full Rietveld refinement profiles for synchrotron ((a) and (b)) and neutron ((c) and (d)) diffraction data collected for* $Bi_{0.95}Dy_{0.05}FeO_3$ *fitted using the Cc space group. The red circles represent the observed data, the green line represents the calculated model and the pink line represents the difference. Full refinements are given in the supplementary information.*

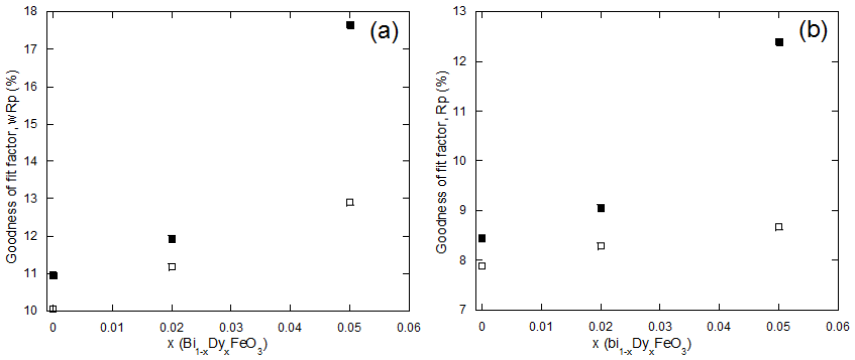

Figure 8: *Comparison of the goodness of fit parameters, wRp (a) and Rp (b) with increasing* Dy^{3+} *content for* $BiFeO_3$, $Bi_{0.98}Dy_{0.02}FeO_3$ *and* $Bi_{0.95}Fe_{0.05}O_3$ *for synchrotron diffraction refinements performed using the R3c (closed squares) and Cc (open squares) models showing the substantially improved fit using the Cc model for* $Bi_{0.95}Fe_{0.05}O_3$.

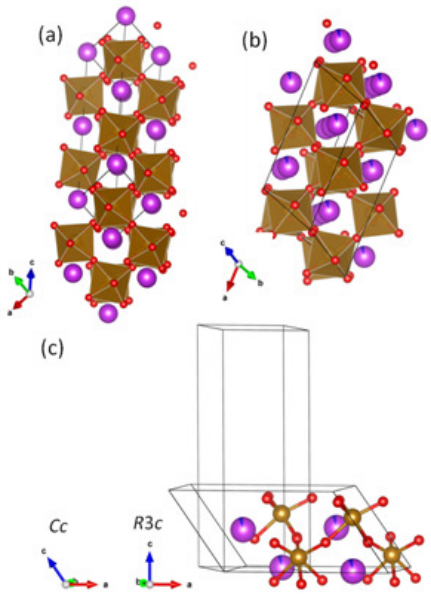

Figure 9: *Schematic representation of (a) the R3c unit cell, (b) the Cc unit cell and (c) the relationship between the two unit cells produced using the VESTA software.*[58] *Where the brown spheres represent the iron atoms, the red spheres represent the oxygen atoms and the purple spheres represent the* Dy^{3+}/Bi^{3+} *ions respectively. The brown squares represent the* FeO_6 *octahedra.*

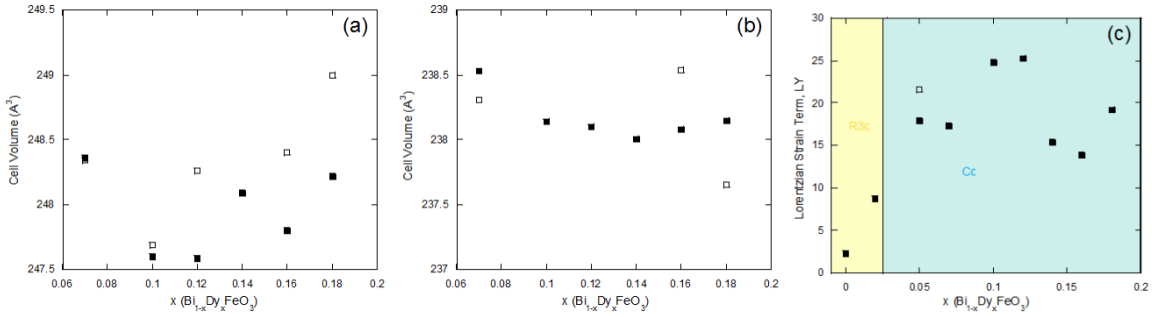

Figure 10: *Variation of (a) cell volume of the Cc phase, (b) cell volume of the (main) Pnma phase and (c) Lorentzian stain term (LY) of the R3c and Cc phases for increasing dysprosium contents showing decreasing cell volume and increasing strain of the Cc phase up to approximately x = 0.12. In (a) and (b) the filled and open symbols are the data taken from synchrotron X-ray and neutron diffraction refinements. In (c) the open symbol gives the value for the LY term associated with the R3c phase showing the decrease in the strain term between R3c and Cc models for* $Bi_{0.95}Dy_{0.05}FeO_3$.

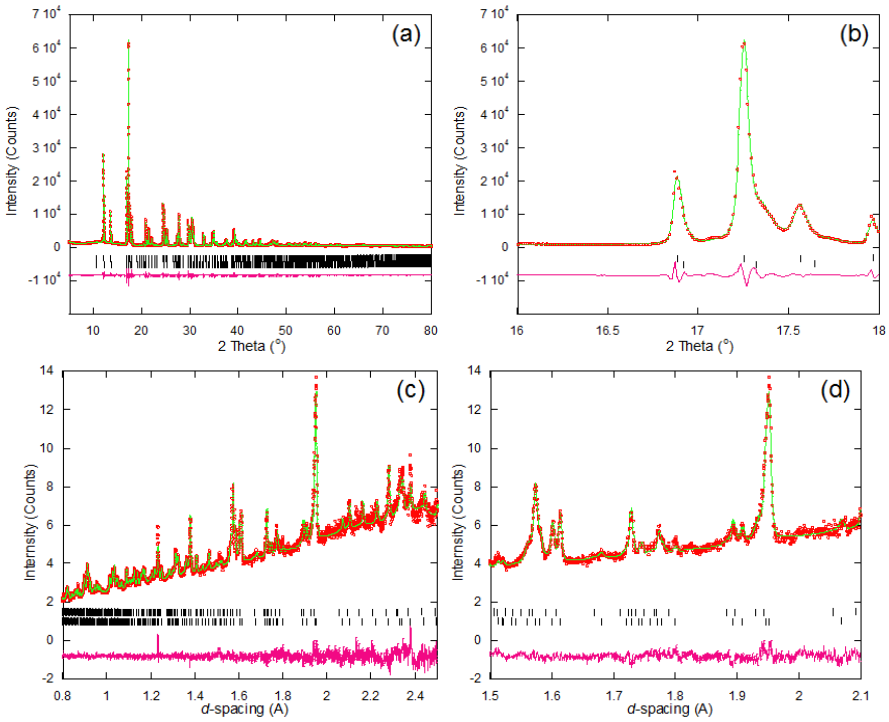

Figure 11: *Full Rietveld refinements profiles for refinements performed on synchrotron ((a) and (b)) and neutron ((c) and (d)) diffraction data collected for* $Bi_{0.70}Dy_{0.30}FeO_3$ *fitted using two Pnma phases with different lattice parameters. The red circles represent the observed data, the green line represents the calculated model and the pink line represents the difference.*

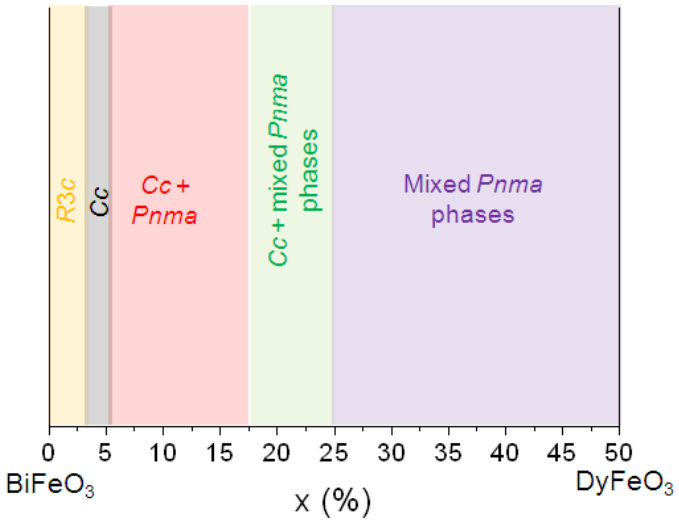

Figure 12: *Proposed phase diagram for* $Bi_{1-x}Dy_xFeO_3$ *ceramics based on powder diffraction studies.*

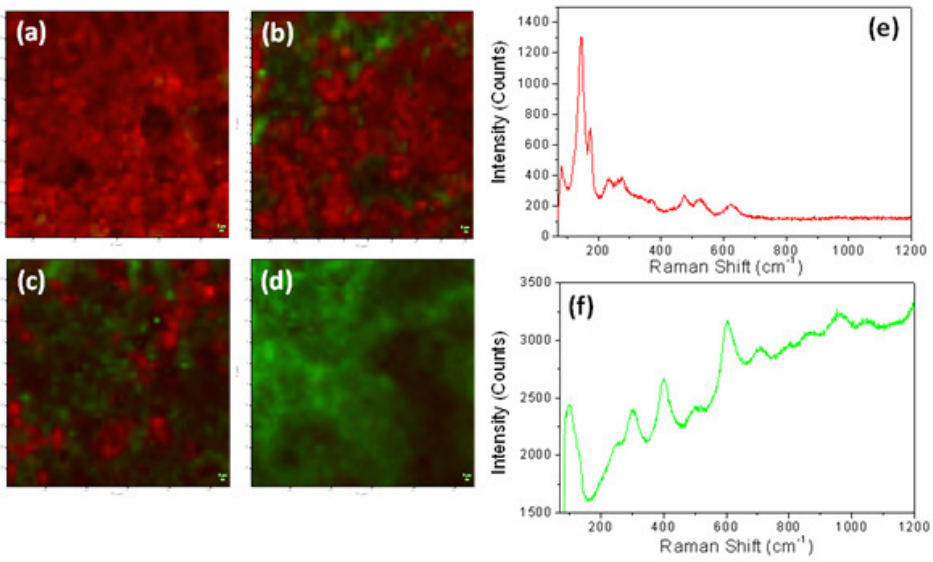

Figure 13: *Raman maps collected at room temperature for (a) $Bi_{0.95}Dy_{0.05}FeO_3$, (b) $Bi_{0.86}Dy_{0.14}FeO_3$, (c) $Bi_{0.82}Dy_{0.18}FeO_3$, (d) $Bi_{0.70}Dy_{0.30}FeO_3$, (e) shows a typical spectrum collected for $Bi_{0.95}Dy_{0.05}FeO_3$ and (f) shows a typical spectrum collected for $Bi_{0.70}Dy_{0.30}FeO_3$. Limits were set in the Raman shift between approximately 100 and 160 cm^{-1} and 560 and 660 cm^{-1} to define contributions from the R3c/Cc and Pnma phases respectively.*

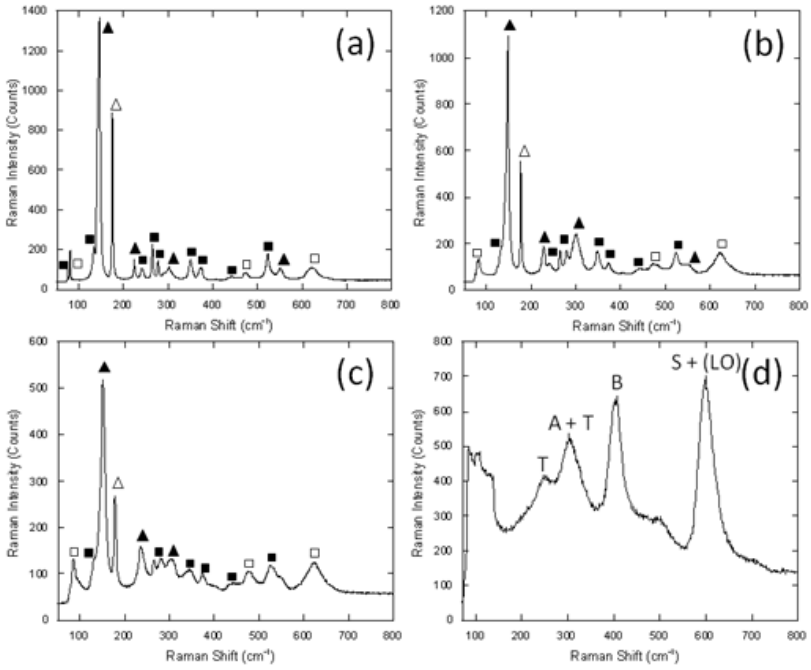

Figure 14: *Raman spectra collected at 80 K for (a) $BiFeO_3$, (b) $Bi_{0.98}Dy_{0.02}FeO_3$, (c) $Bi_{0.95}Dy_{0.05}FeO_3$, and (d) $Bi_{0.70}Dy_{0.30}FeO_3$. Assignments were made based on the work by Hlinka et. al. and Bielecki et. al.[9, 50] Adopting the notation from Hlinka et. al. filled square symbols represent E(TO) modes, open square symbols represent E(LO) modes, filled triangular symbols represent A_1(TO) modes and open triangular symbols represent A_1(LO) modes respectively.[50] For $Bi_{0.70}Dy_{0.30}FeO_3$ the Raman modes are denoted by A, T, B and S which represent A-site, oxygen tilt, oxygen bending and oxygen stretch modes respectively as reported by Bielecki et. al.[9]*

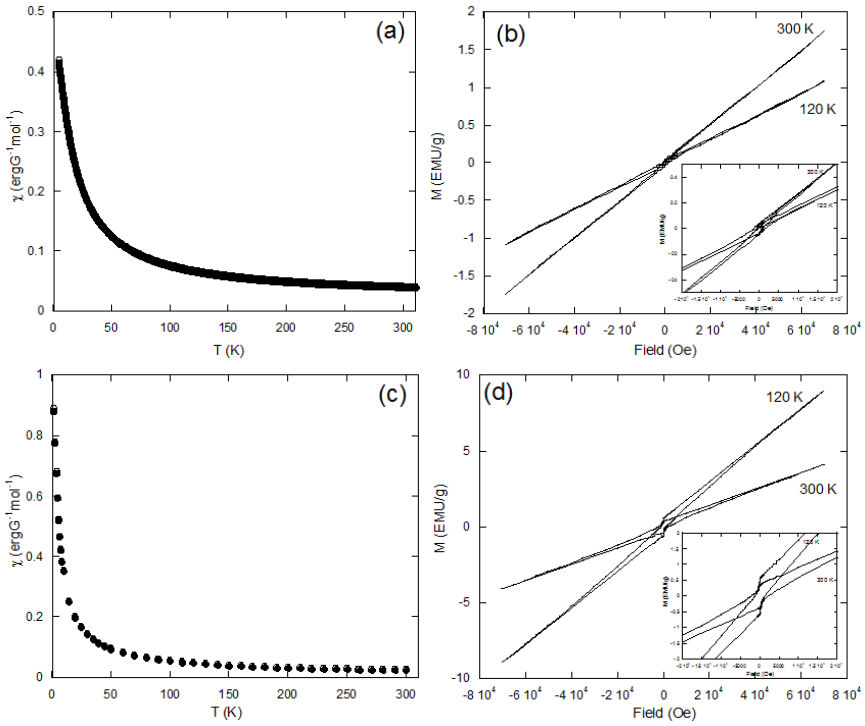

Figure 15: *SQUID magnetometry data (a) zero field cooled/field cooled data and (b) field dependent data collected for* $Bi_{0.95}Dy_{0.05}FeO_3$*. The inset to (b) shows a zoomed in portion of the hysteresis loop showing weak hysteresis. (c) zero field cooled/field cooled data and (c) field dependent data collected for* $Bi_{0.70}Dy_{0.30}FeO_3$*. The inset to (d) shows a zoomed in portion of the hysteresis loop showing weak hysteresis.*

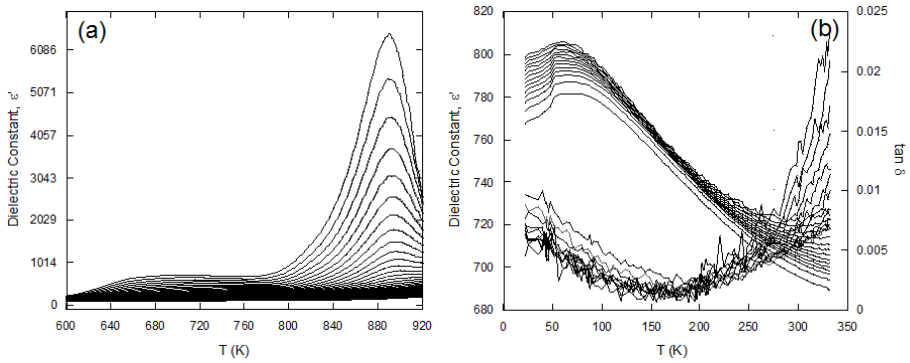

Figure 16: *Electrical measurements collected for (a)* $Bi_{0.95}Dy_{0.05}FeO_3$ *showing an anomaly in the dielectric constant at approximately 675 K consistent with a magnetic ordering transition and high permittivity relaxor-like character typical of non-ohmic electrode effects arising from the 'leaky' dielectric characteristics of the material and (b)* $Bi_{0.70}Dy_{0.30}FeO_3$ *showing relaxor-type behaviour at approximately 100 K.*

List of Tables

Table 1: *Lebail refinement details for the analysis of powder neutron and synchrotron diffraction data collected for $Bi_{0.95}Dy_{0.05}FeO_3$, refined using the parent R3c model and the monoclinic, Cc and triclinic, P1 models proposed by symmetry mode analysis.*

Parameter	**Symmetry**					
	Synchrotron Data			**Neutron Data**		
	R3c	**Cc**	**P1**	**R3c**	**Cc**	**P1**
R_{wp} **(%)**	15.62	11.59	9.48	8.55	6.35	5.09
R_p **(%)**	10.90	8.02	5.99	9.06	6.43	5.08
a **(Å)**	5.57452(5)	9.6547(1)	5.57457(5)	5.5743(1)	9.6518(2)	5.57493(7)
b **(Å)**	5.57452(5)	5.57640(6)	5.57362(5)	5.5743(1)	5.5774(1)	5.56521(8)
c **(Å)**	13.8534(2)	5.62527(7)	5.63243(4)	13.8510(4)	5.6365(1)	5.6373(1)
Cell Vol. (Å^3)	372.823(7)	248.635(5)	124.281(2)	372.72(2)	248.65(1)	124.289(4)
α, β, γ	90 90 120	90 124.8177(7) 90	60.2432(6) 60.3021(6) 60.0295(6)	90 90 120	90 124.9665(9) 90	60.3172(6) 60.1950(7) 60.1476(6)

Table 2: *Full refinement details for both the powder neutron and synchrotron diffraction data collected for* $Bi_{0.95}Dy_{0.05}FeO_3$ *modelled using the monoclinic, Cc, space group. Goodness of fit parameters are wRp = 7.03 % and Rp 8.00 % for neutron diffraction data and* R_{wp} *= 11.65 % and* R_p *= 8.52 % for synchrotron diffraction data respectively. Note: the oxygen atomic sites and thermal contributions remain fixed for the refinements of the synchrotron diffraction data.*

Parameter	Neutron Data	Synchrotron Data
a **(Å)**	9.6447(3)	9.6492(2)
b **(Å)**	5.5768(2)	5.57676(8)
c **(Å)**	5.6323(2)	5.63255(7)
Cell Vol. (Å^3)	248.23(1)	248.451(7)
γ **(°)**	124.975(2)	124.944(1)
Bi/Dy (*0*, *¼*, *0*)		
Bi/Dy Ui/Ue*100	0.78(4)	1.063(20)
Fe (*x*, *y*, *z*)	0.2229(4) 0.2611(5) 0.6665(3)	0.2249(8) 0.257(2) 0.6649(6)
Fe U_{iso}	0.36(4)	-0.11(6)
O1 (*x*, *y*, *z*)	-0.0340(7) 0.178(1) 0.360(1)	-0.034001 0.178235 0.359604
O1 U_{iso}	0.55(9)	1.00
O2 (*x*, *y*, *z*)	0.1640(7) 0.477(1) -0.149(1)	0.163979 0.476745 -0.148575
O2 U_{iso}	0.8(1)	1.00
O3 (*x*, *y*, *z*)	0.2373(8) -0.0379(9) -0.124(1)	0.237289 -0.037871 -0.123368
O3 U_{iso}	0.7(1)	1.00
Bi-O1 lengths (Å)	2.265(5) 2.478(6)	2.26532(3) 2.47772(3)
Bi-O2 lengths (Å)	2.514(7) 2.270(5)	2.51390(2) 2.27070(3)
Bi-O3 lengths (Å)	2.360(5) 2.507(6)	2.36180(4) 2.50807(4)
Fe-O1 bond lengths (Å)	2.105(6) 1.968(6)	2.114(6) 1.955(7)
Fe-O2 bond lengths (Å)	1.880(6) 2.110(6)	1.91(1) 2.116(8)
Fe-O3 bond lengths	2.003(5) 2.120(5)	1.99(1) 2.090(9)
Fe-O1-Fe bond angle (°)	152.3(3)	152.9(1)
Fe-O2-Fe bond angle (°)	152.6(3)	151.9(4)
Fe-O3-Fe bond angle (°)	158.6(3)	159.5(2)

Table 3: *List of Raman mode frequencies for x = 0, 0.02, 0.05 and 0.30 $Bi_{1-x}Dy_xFeO_3$ materials obtained at 80 K. Assignments were made based on the work by Hlinka et. al. and Bielecki et. al.[9, 50] Where TO are Raman active transversal optic modes and LO are Raman inactive longitudinal optic frequencies which become Raman active due to Fröhlichs leading to strong second order interactions. A_1 and E are irreducible representations of the crystal structure for R3c(Cc) symmetries. For the Pnma symmetry the Raman modes are denoted by A, T, B and S which represent A-site, oxygen tilt, oxygen bending and oxygen stretch modes respectively.*

Material	**Raman modes**[9, 50]			
	E(TO)	**E(LO)**	**A_1(TO)**	**A_1(LO)**
$BiFeO_3$	75.1 133.9 241.6 264.9 278.9 349.7 373.7 442.2 523.1	80.5 475.6 621.3	147.4 224.2 301.7 551.5	176.1
$Bi_{0.98}Dy_{0.02}FeO_3$	241.0 265.2 278.9 348.4 373.4 442.8 522.5	82.9 472.4 620.4	147.7 227.1 301.3 549.0	177.4
$Bi_{0.95}Dy_{0.05}FeO_3$	266.5 279.9 347.2 374.0 443.8 524.7	85.0 475.2 620.4	152.4 236.7 304.9	179.1
	Raman modes[9]			
	A	**T**	**B**	**S**
$Bi_{0.70}Dy_{0.30}FeO_3$	301.6	247.8 301.6	405.7	600.0